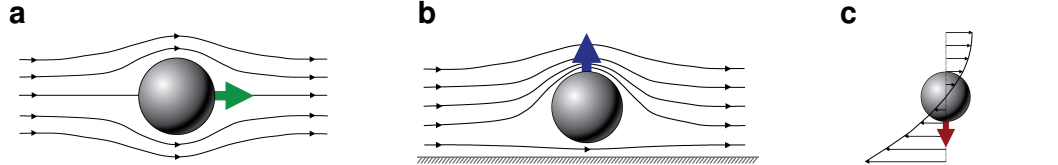


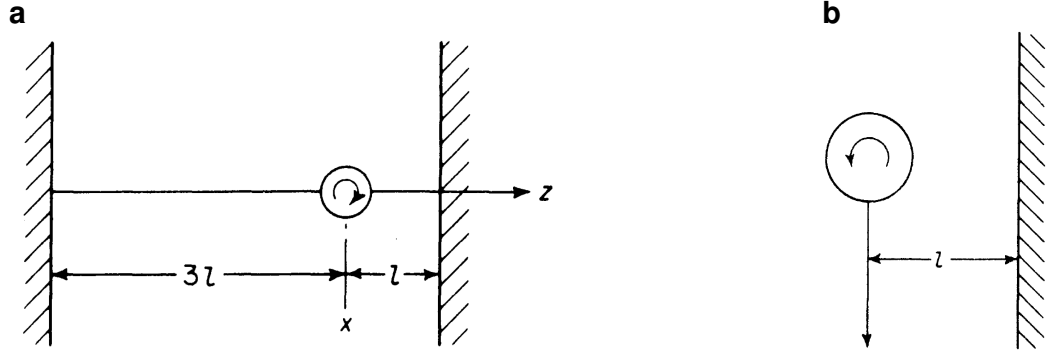
Figure 1: Force Balance on a Rolling Particle with Bio-Functionalization

Bla



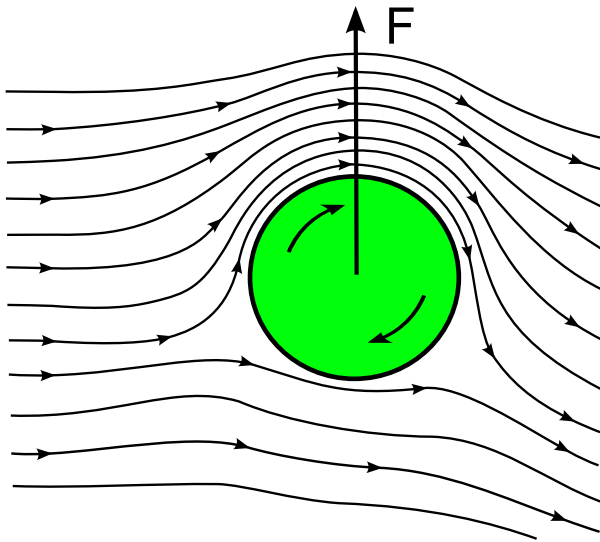
**Figure 2: Particle Drag and Lift Behavior**

(a) Bulk Drag: Force acts on a particle caused by the displacement of fluid stream lines. (b) Wall-lift Drag Force: In a special case of drag, where streamlines cannot be displaced further, a pressure gradient forms in front of the sphere. This forces a motion directed perpendicularly from the wall. (c) Shear-induced force: The curvature of the flow profile exhibits a translation and rotation due to inhomogeneously distributed shear on the surface.[22]



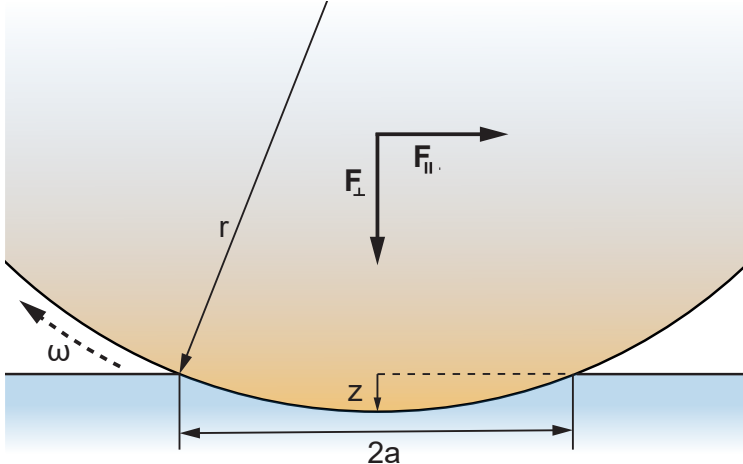
**Figure 3: Particle Rotation Behavior**

(a) Direction of rotation of a sphere settling in eccentric position between parallel walls. (b) Direction of rotation of a sphere settling in the presence of a single plane wall far from the other side.[21]



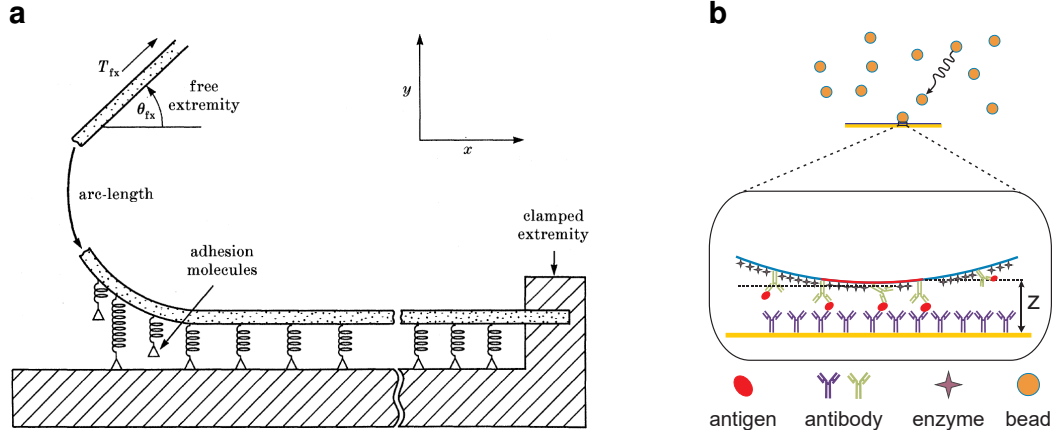
**Figure 4: Magnus Effect on a Particle in Laminar Flow**

The intrinsic rotation of a particle inside a laminar flow field causes a pressure gradient to the side whose tangential rotation vector is parallel to the stream lines.



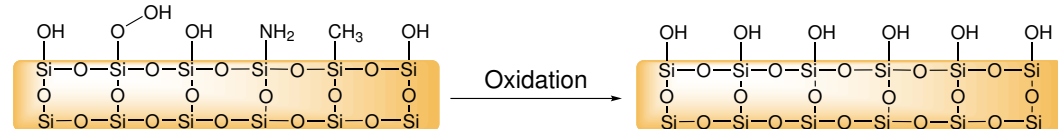
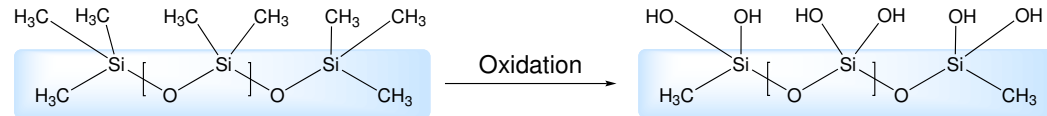
**Figure 5: Rolling Mechanics of a Sphere**

Penetration model of a sphere with radius  $r$  adapted from Azad and Featherstone [38] and Waters and Guduru [39]. The top body moves into the elastic bottom body for an approach ( $z$ ) and a contact area  $\pi a^2$ .



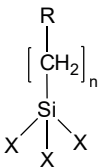
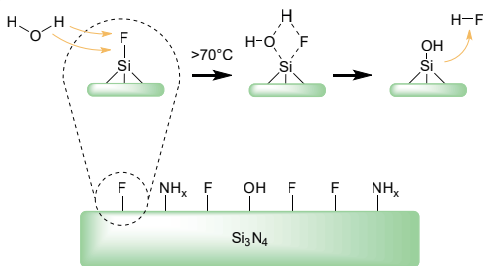
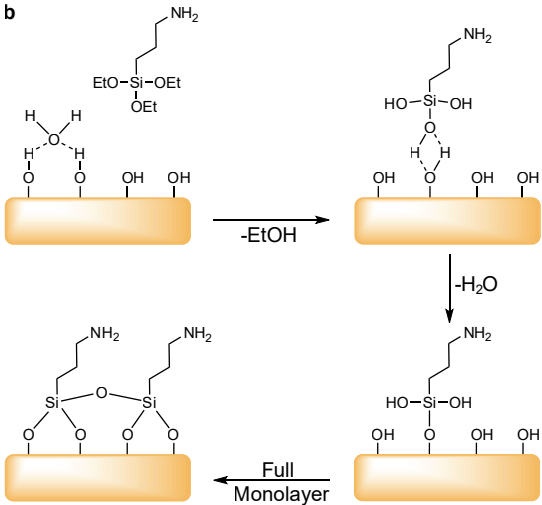
**Figure 6: Membrane Adhesion and Detachment Models**

**a** Adhesion Model after Dembo et al. [42]: Every interaction is viewed as spring-damper-model in superposition. **b** Surface Coverage Assay Model: In a stochastic approach, analyte molecules and their interactions are modeled between a planar and a spherical surface. Adapted from Wu and Voldman [20]

**a****b**

**Figure 7: Different Substrate Surfaces: Glass, PDMS and Si<sub>3</sub>N<sub>4</sub>**

Surface groups and internal structure of quartz glass (**a**), PDMS (**b**), and silicon nitride (**c**). After an oxidation step, the methyl groups are converted to hydroxyl.

**a****c****b**

**Figure 8: Surface Oxidation and Modification by APTES**

(a) Structure of a typical trialkoxysilane, X: hydrolyzable group, R: non-hydrolyzable organic radical, n: methylene chain-length. (b) Before the condensation reaction, the oxidized surface has formed hydrogen bonds with water molecules while the silane molecules are in the bulk solution. The hydrolyzed silanol group adsorbs onto the surface and forms hydrogen bridges with the silicon bound oxygen atom. In a condensation reaction, under the loss of water, a covalent bond to the surface forms. After the SAM assembly the surface is saturated with a covalent-bound, crosslinked silane film.[75] (c) Proposed oxidation of  $\text{Si}_3\text{N}_4$  with HF: Due to similar activation energies water can displace HF in a competitive manner effectively above a temperature above 70 °C.

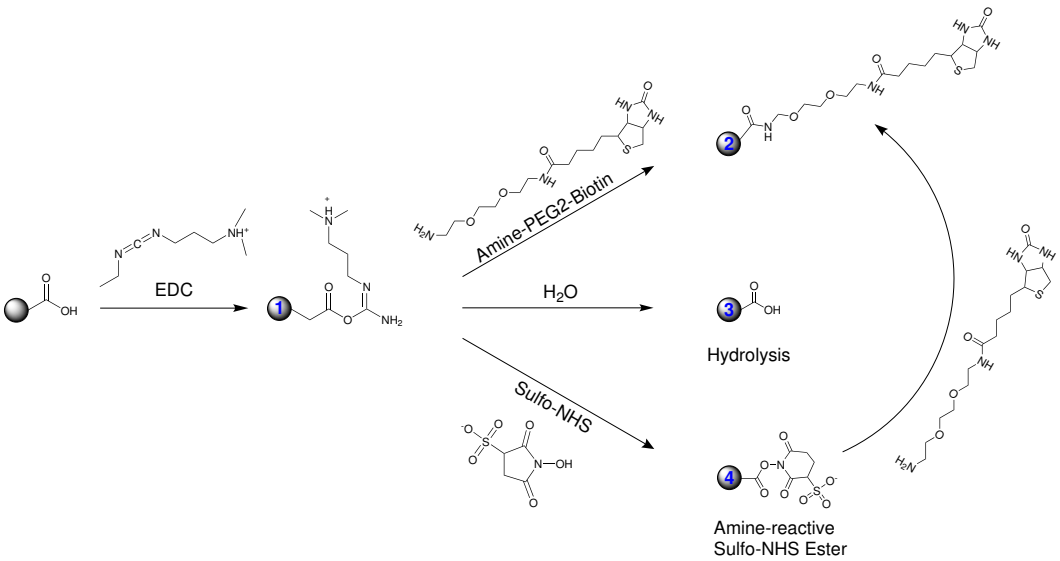


**Figure 9: Carboxyl bead modification with EDC/NHS**

The carboxyl groups on the bead are activated with EDC to an active O-acylisourea intermediate. This can then either be nucleophilically attacked by a primary amine of the amine-PEG<sub>2</sub>-biotin reactant or - due to its instability - hydrolyzed back to a regenerated carboxyl surface. A present NHS-ester can also displace the O-acylisourea to form a considerably more stable intermediate which then itself reacts with any primary amine.

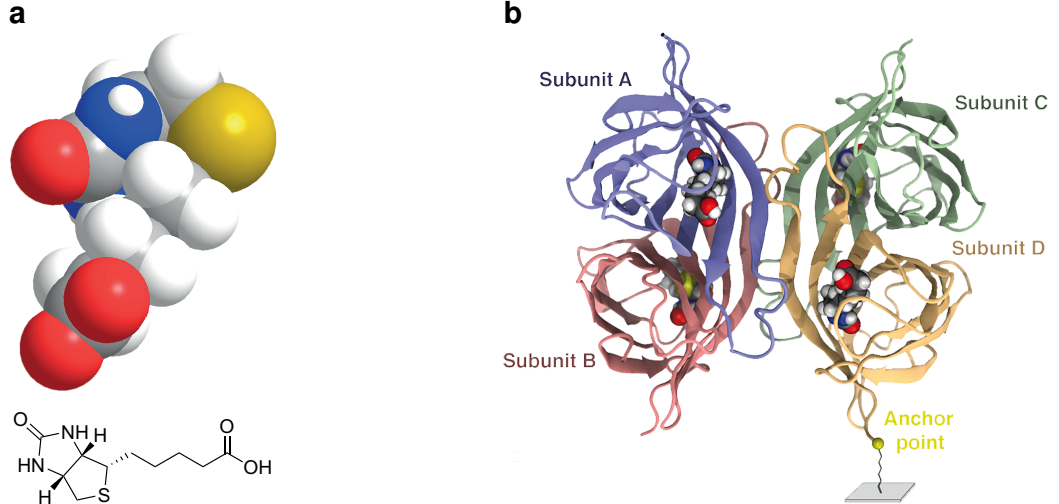


**Figure 10: Functional Structures of Biotin and Streptavidin**

(a) Two- and three dimensional chemical structure of the biotin molecule. (b) Homotetrameric streptavidin with four subunits and four bound biotin-ligands. The molecule is attached with the anchor point at one terminus to a surface.[91]

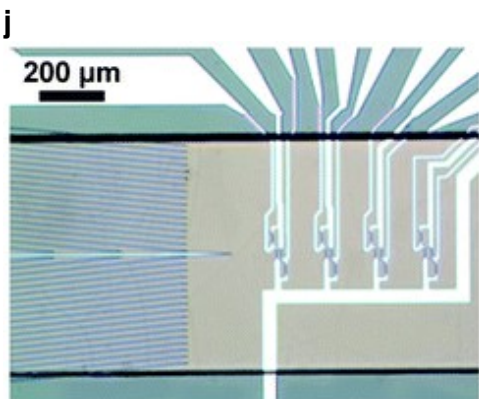
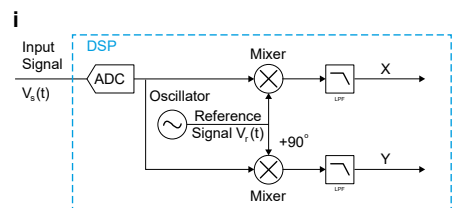
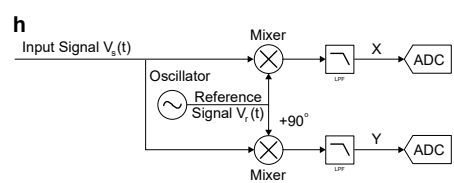
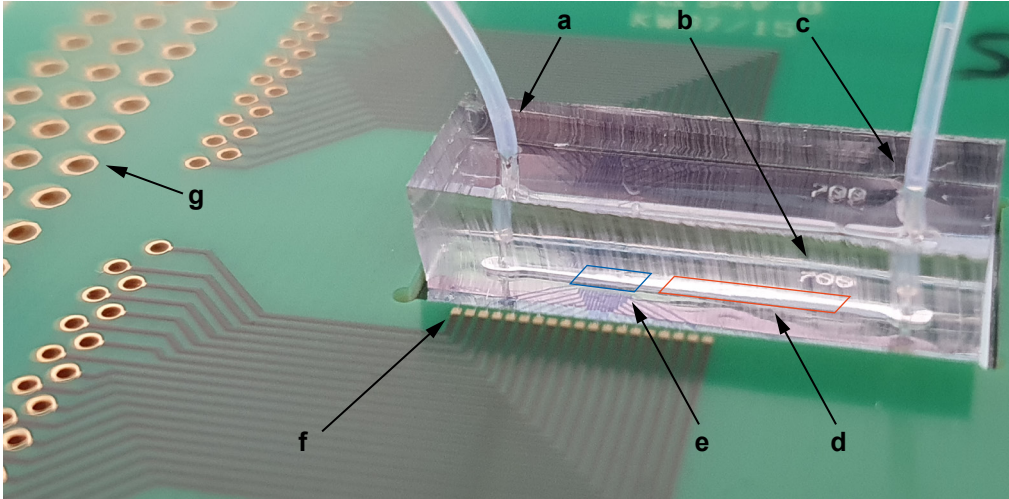


**Figure 11: Overview over the MRCyte Sensor Setup**

(a) Microfluidic outlet connection to waste reservoir. (b) Imprinted channel width. (c) Microfluidic inlet connection to syringe pump. (d) Magnetophoretic focusing region, not visible in this picture. (e) GMR-sensor region, the supply and bridge balancing traces are visible. (f) Gold bondpad: In order to connect the silicon sensor chip with the breakout printed circuit board (PCB), wedge bonds from the chip pads to the PCB pads are forged. (g) Through hole plating for the connection to the lock-in via jumper cables or a soldered connector plug. (h) Typical signal processing flow of a lock-in. The reference signal  $V_r(t)$  is splitted and mixed with the input signal with a phase difference of  $0^\circ$  and  $90^\circ$ . Then, both signals are low-pass filtered and sampled by an analog-to-digital converter (ADC). (i) Accordingly, in a digital signal processing (DSP) device the input signal is digitally converted beforehand, which in turn requires a highly sensitive and fast ADC. In contrast, DSP is more accurate and allows for software-controllable technical opportunities. (j) GMR-sensor bridge circuit inside the microfluidic channel. On the left hand side, magnetophoretic focusing structures are visible. On the right hand side, four Wheatstone bridges on a compliant ground plane can be observed.

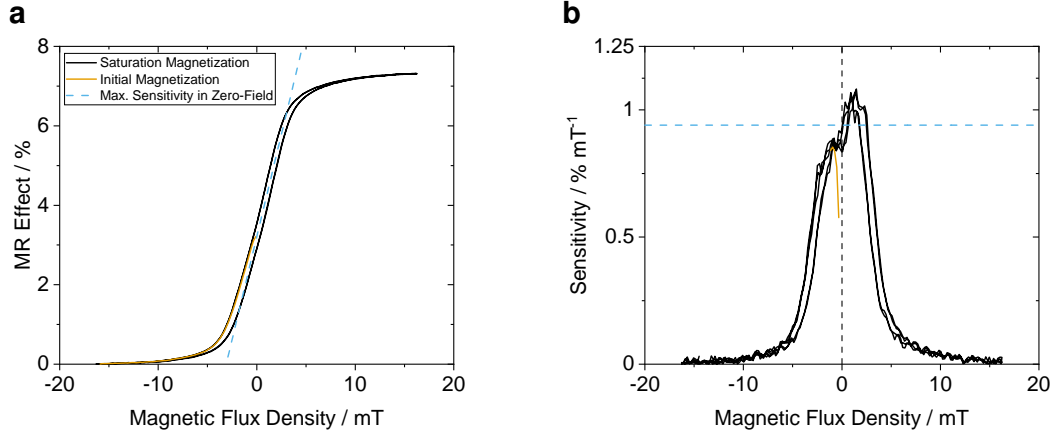


**Figure 12: Hysteresis Calibration of the GMR-Sensor**

Sensitivity Optimization of the GMR sensor via alternating hysteresis measurements and permanent magnet adjustment. (a) Optimal sensitivity is reached when the zero-crossing is centered around the zero-field and the linear section has the maximum steepness. (—) Upon dislocating the free layer in one direction, the magnetic field strength increases linearly towards saturation. (—) Afterwards, the magnetization moves on the hysteresis loop. The total magneto-resistive effect (MR effect) is calculated from the vertical distance between the saturation points. (—) (b) In order to determine the steepness in the linear section, the hysteresis from the left side is differentiated. Actual sensitivity (—) is measured by the mean of all curves in the zero field. The initial magnetization curve is omitted from this measurement. (—)

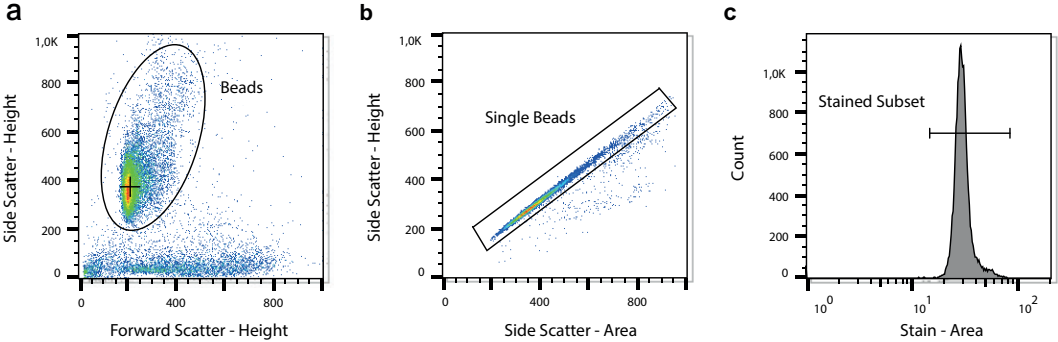


**Figure 13: Gating Strategy for Biotinylated Beads**

- a**, In the forward-side-scatter plot, the general bead population with high side scatter is selected from the background.
- b**, Single beads are differentiated by their sphericity, their ratio of height:area in the side scatter. Points on the line through the origin are spherical. **c**, The stained subset in the respective color is now selected and the median fluorescence intensity (MFI) as well as the coefficient of variance (CV) is computed.

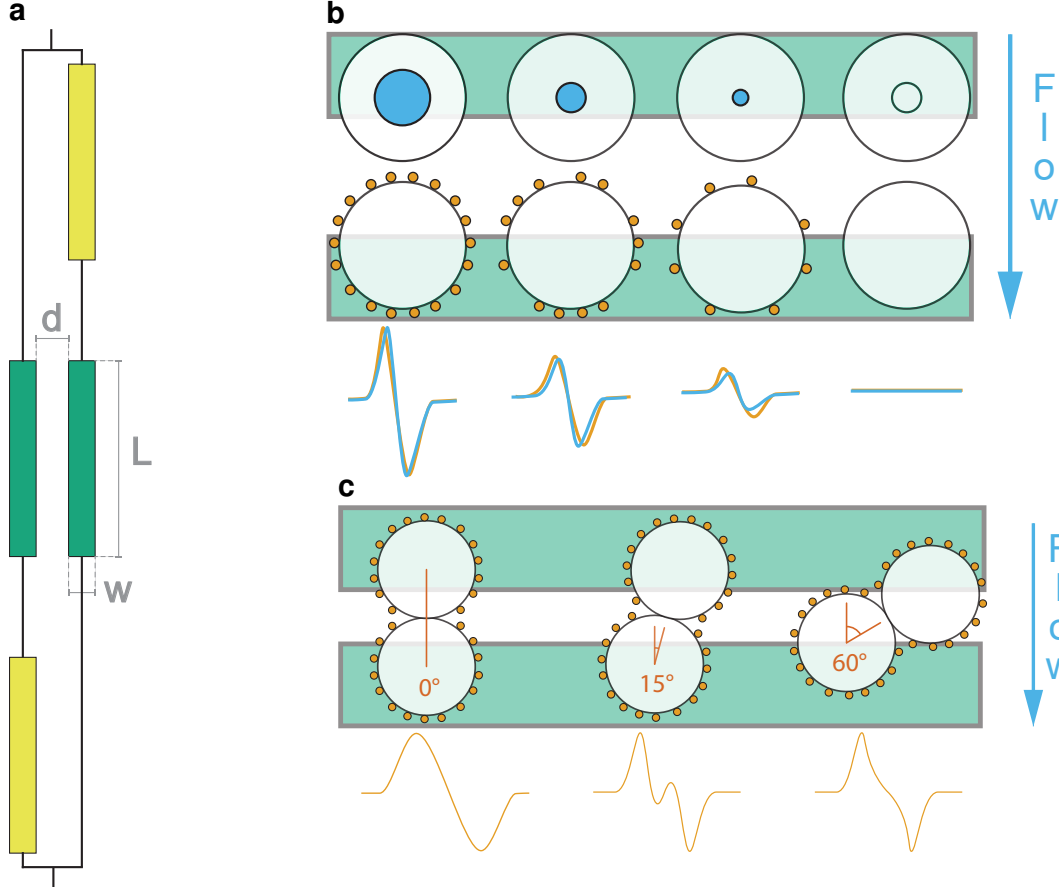


**Figure 14: Particle Coverage Simulation**

(a) Dimensions of the GMR Wheatstone bridge sensor: Distance  $d$  between both variable bridges (green), width  $w$  of a GMR-sensor, length  $L$  of a sensor. (b) Scheme of single cell simulation: The ideal magnetic dipole in the geometric center of a sphere (●) causes a signal deviation from the real cell signal with magnetic moment distributed on the cell surface (○). (c) Signal shapes of different angles of two-particle aggregates lead to differing signal shapes.

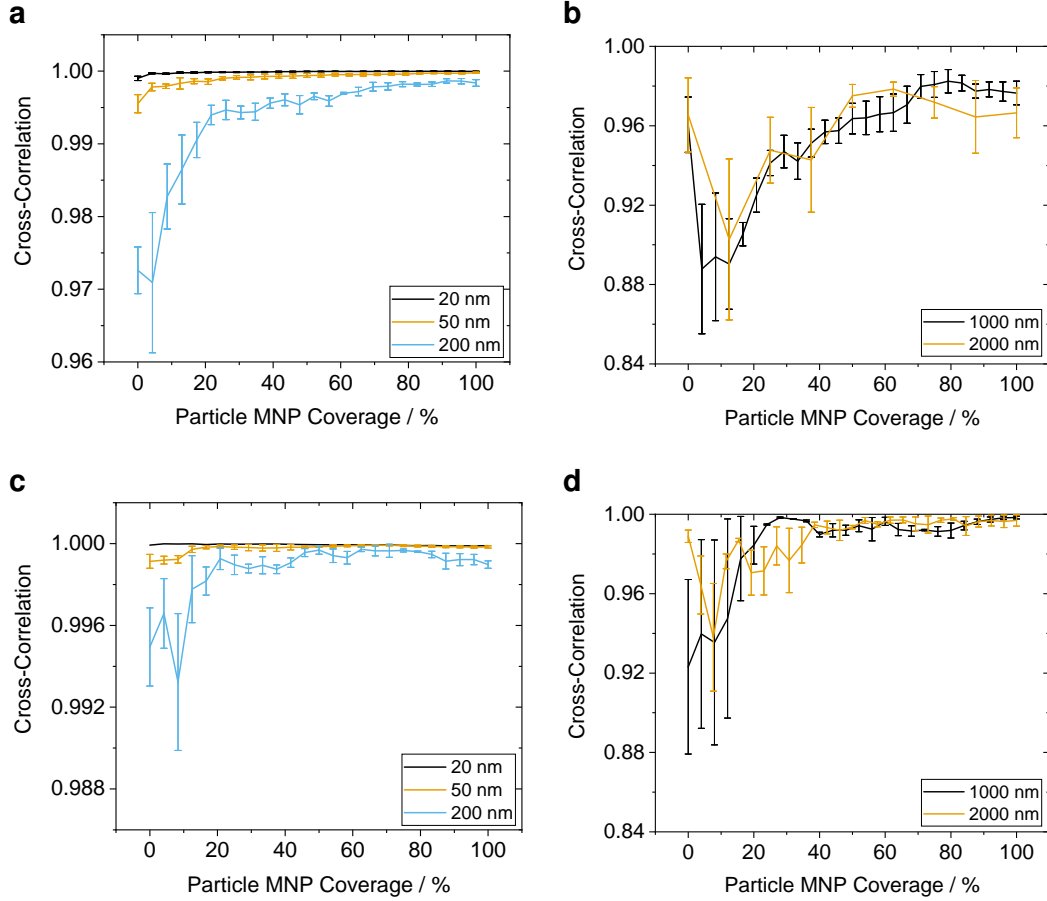


**Figure 15: Coverage Dependent Signal Correlation**

MNP coverage of a sphere with  $4\text{ }\mu\text{m}$  (**a**, **b**) and  $8\text{ }\mu\text{m}$  diameter (**c**, **d**) covered by magnetic particles ranging from  $20\text{ nm}$  to  $2000\text{ nm}$ . A cross-correlation increase which is inversely proportional to the MNP size can be observed.

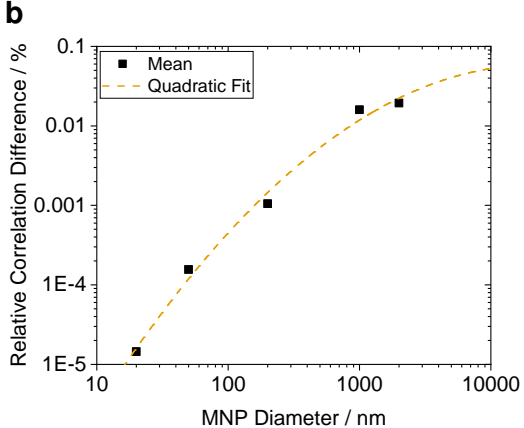
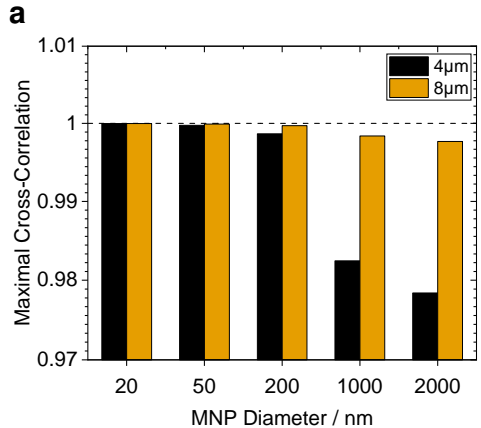


**Figure 16: Maximal Cross-Correlation Differences**

- (a) Mean coverage at 99 % for 4  $\mu\text{m}$  and 8  $\mu\text{m}$  spheres. A negative dependency on the MNP size can be explained by the ratio of magnetic momentum per unit surface and its homogeneous distribution across the whole surface.
- (b) Relative correlation error between 4  $\mu\text{m}$  and 8  $\mu\text{m}$  spheres with a quadratic fit. The quadratic behavior could be related to the relative surface area which can be occupied by magnetic momentum. (Adj.  $R^2 = 0.992\,09$ )

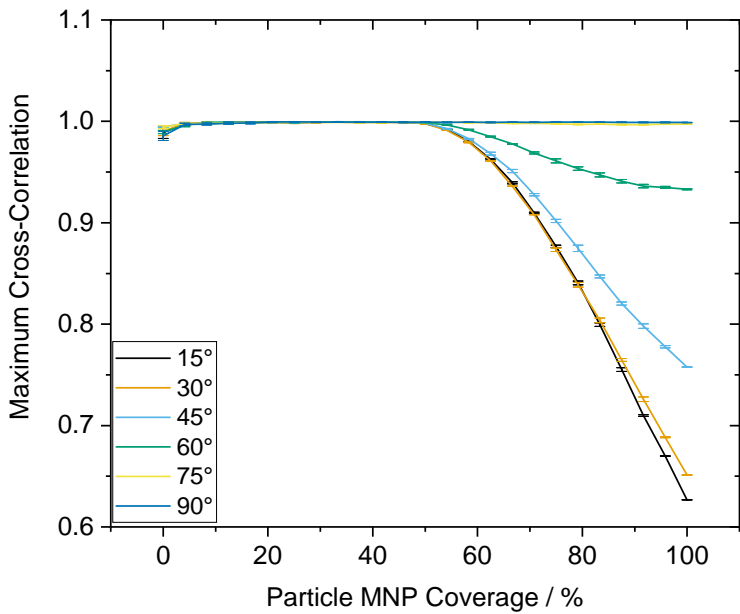


**Figure 17: Signal Correlation between Two-Cell Aggregates At Shifting Angles**

Two-Sphere aggregates are covered with 200 nm MNPs and simulated flowing over the sensor at differing respective angles. The SEM indicates a difference in cross-correlation of three truly random MNP distributions. For low yaw angles and high coverages, the aggregate's signal reflects rather two single dipoles in superposition than one quite homogeneous dipole. This causes a high signal deviation from the reference and thus a low degree of correlation.

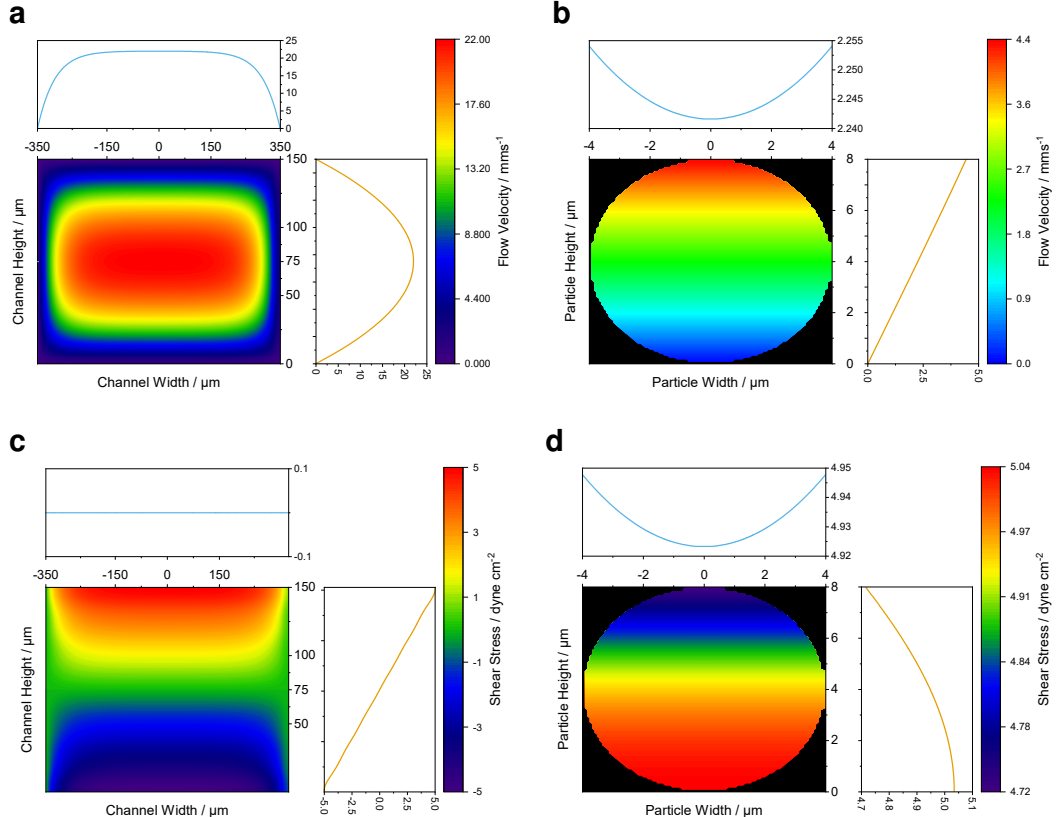


**Figure 18: Flow Field and Shear Stress Simulation of the utilized Microchannel**

Flow (**a**) and vertical shear (**c**) field inside the microchannel with dimensions ( $w \times h \times L$ )  $700 \mu\text{m} \times 150 \mu\text{m} \times 15\,800 \mu\text{m}$  for a flow rate of  $80 \mu\text{L min}^{-1}$  and with neglected tubing effects. The subplots on the right and top side show the mean horizontal and vertical profile in  $0 \mu\text{m}$  width and  $75 \mu\text{m}$  height, respectively. (vertical: —, horizontal: —) Due to the no-slip condition, the velocity at the walls equals zero and the shear is maximal. The maximum of the Hagen-Poiseuille profile is located in the channel center. Over the cross-section the mean flow velocity  $\bar{u}$  equals  $12\,670.83 \mu\text{m s}^{-1}$ . Resultingly, the net horizontal viscous shear  $\tau_{viscous} = \frac{\partial u}{\partial z}$  cancels out over the whole channel cross-section.

Flow (**d**) and vertical shear (**d**) field acting on a  $8 \mu\text{m}$  diameter bead on the channel bottom. The mean fluid velocity trapped by the bead profile results in  $\bar{u}_p = 2241.59 \mu\text{m s}^{-1}$ , whereas the viscous shear strains with  $\tau_{viscous} = 4.93 \text{ dyne cm}^{-2}$ .

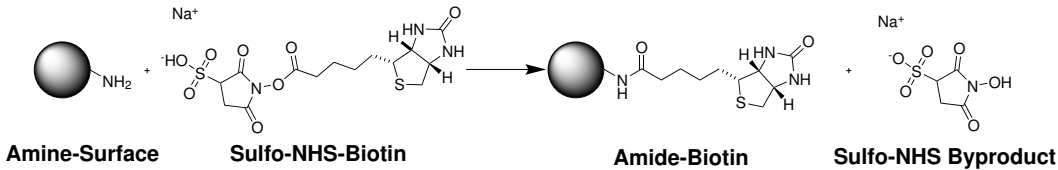


**Figure 19: Amine Bead Modification with Sulfo-NHS-Biotin**

An amine terminated bead brought into reaction with sulfo-NHS-biotin. Both form an amide linkage and bind biotin covalently to the surface. As byproduct the sulfo-NHS-ester splits off.

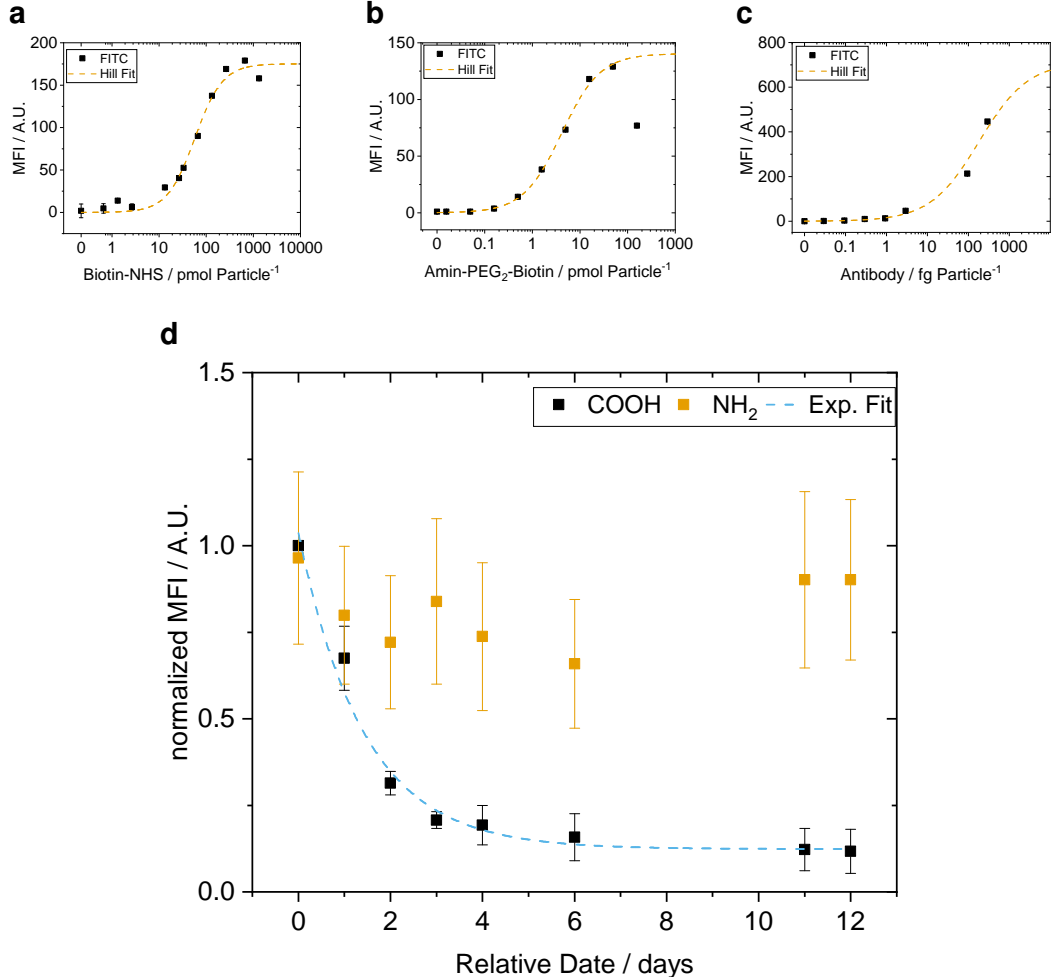


**Figure 20: Titration of Biofunctional Molecules on 8  $\mu\text{m}$  Particles**

Titration curves of NHS-biotin (a), Amin-PEG<sub>2</sub>-Biotin (b), and Anti-IgG1 (c) with their respective Hill fits. The corresponding fit parameters as well as the goodness factor are shown in ???. (d) Stability analysis of functionalized carboxyl and amine beads over 12 days. The carboxylate particles show a exponential decrease with a half-life of 1.43 days as determined by the exponential fit. The respective parameters are shown in ???.

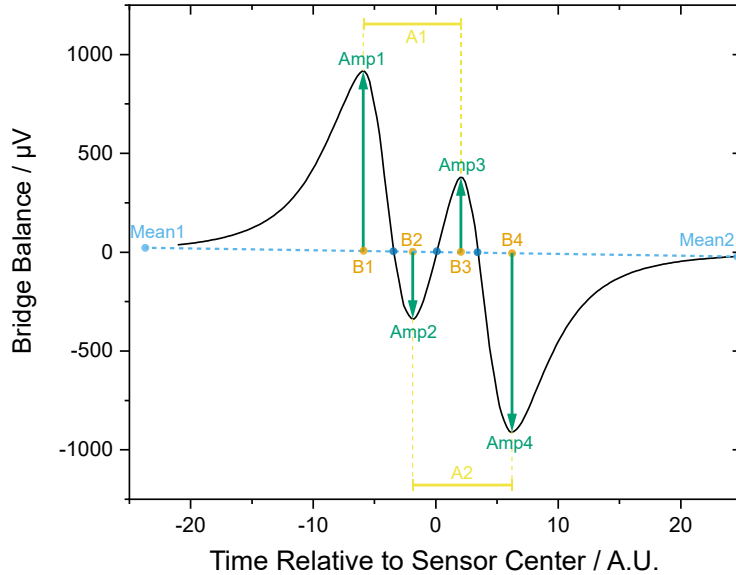


**Figure 21: Example Signal of Magnetic Measurement**

Signals generated from the Wheatstone bridge sensor setup feature a certain shape which allows for several measures. In case the overall signal stream carries a constant or linear offset, it is scaled to the means before and after the detected peak pattern. (Mean1, Mean2) The x- and y-positions of each peak are denominated by B1-4 and Amp1-4, respectively. The crossings of the signal through the linear connection of both means are denominated by n1-3 (in the figure by ●). Further, the difference between the equally oriented peaks B3-B1 and B4-B2 give a measure for the homogeneous movement of the measured object and are called A1 and A2 each. From these values the overall velocity  $v$  can be approximated because the GMR bridge distance ( $d_{\text{GMR}}$ ) and sampling frequency ( $f_s$ ) is fixed precisely. Analogously, the magnetic diameter of a dipole is computed by the mean of the differences B2-B1 and B4-B3.

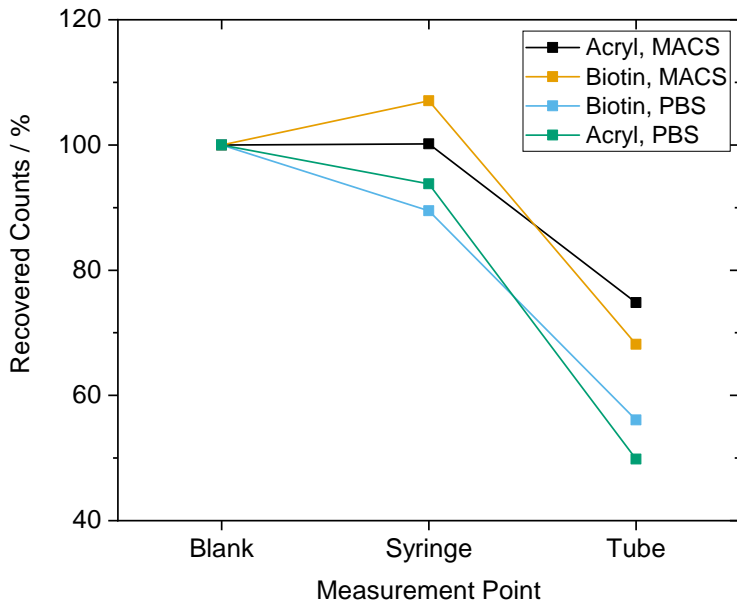


**Figure 22: Bead Loss Evaluation in Connectors**

Bead concentrations measured in equal volumes in the flow cytometer after being pumped through a syringe or a syringe with connected tubing. The blank sample was measured directly from the stock solution. Additionally, electrostatic and surface tension related effects were resolved by the usage of different buffers and bead surfaces.

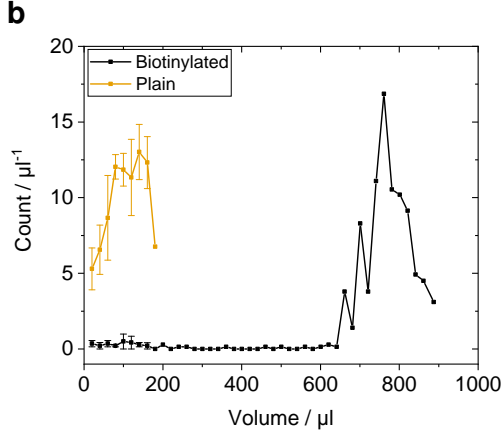
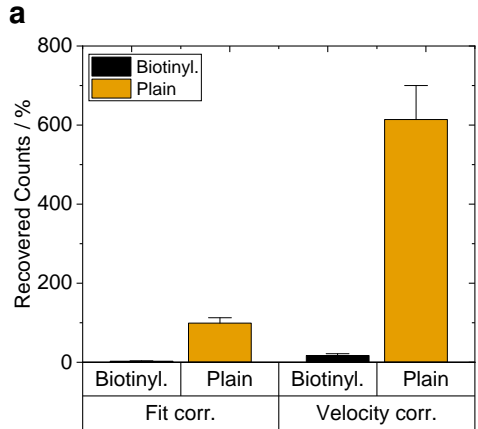


**Figure 23: Error Sources in Concentration Measurements**

(a) Robustness evaluation of the both correction factors  $C_{\text{const}}$  and  $C_{\text{velocity}}$  for protein coated surfaces. The mean and SEM of plain and biotinylated measurements show a high deviation from physically reasonable expectations when corrected for the velocity (right). In contrast,  $C_{\text{const}}$  can intrinsically correct only well below 100 %. (b) Mean and SEM of a fit-corrected bead capture experiment with several error sources. Initially, the magnetophoretic structures have to be filled and thus decrease the plain count for the first 100  $\mu\text{L}$ . (—) Additionally, the high deviation offsets the correction factor so that the stable measurement from 100  $\mu\text{L}$  to 200  $\mu\text{L}$  lies now above the ideal reference. In contrast, the biotinylated beads are captured by the surface functionalization and hence a very low concentration is measured. However, a steep rise with pulsations can be observed when the surface is saturated with beads and the particles begin to flow over the sensor in bursts. (—) The abrupt decline to the end of the measured volume is most probably related to sedimentation effects inside the emptying syringe.

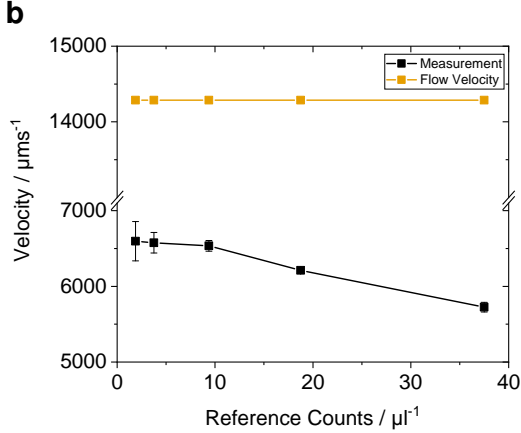
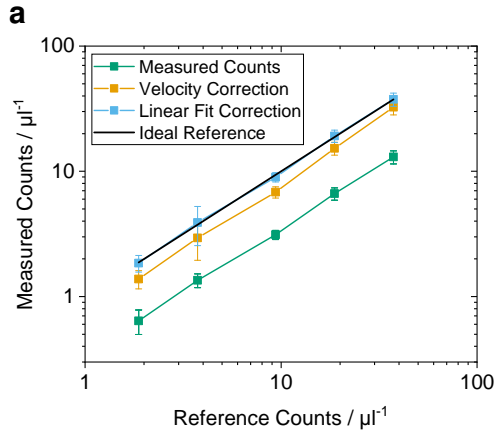


**Figure 24: Absolute Concentration Measurements**

(a) Mean and standard deviation of the concentration measurement from three independent measurements. The uncorrected measurement shows a highly reproducible and linear count over the dynamic range of almost two decades. (—■—) The ideal reference from the flow cytometer is depicted in (——). Correction with  $C_{\text{velocity}}$  (—■—) yields at a factor of 2.261 09 which is 21.7 % more imprecise than  $C_{\text{const}}$  at  $2.888\,33 \pm 0.080\,75$ . (—■—) (b) Mean and SEM of the  $v_c$  estimation from the signal. For higher concentrations, the measured velocity becomes inaccurate thus distorts the correction factor.

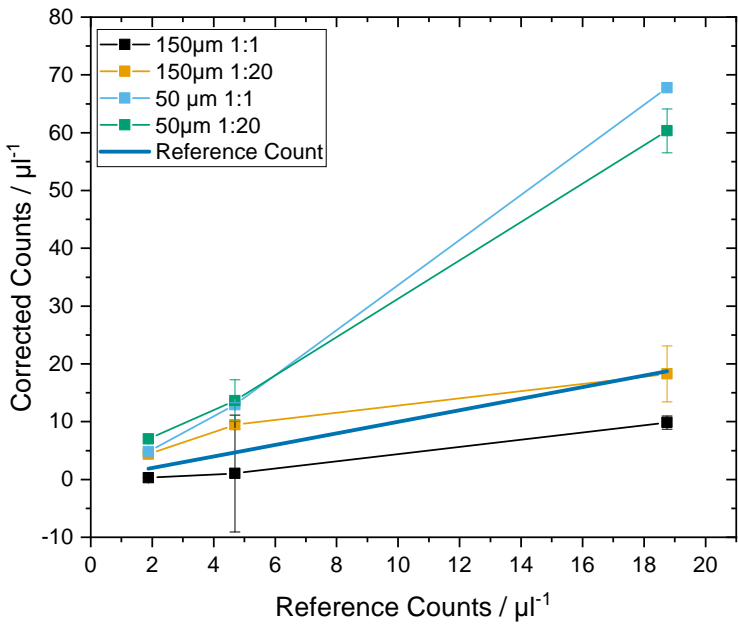


**Figure 25: Absolute Concentration Measurement in Blood Samples Under Varying Channel Height**

Velocity corrected concentration measurements for two different blood dilutions and channel heights. While  $C_{\text{velocity}}$  works for high channels in all tested concentrations, it does not work for high concentrations in 50  $\mu\text{m}$  high channels. This is probably a result of bead-cell collisions and the resulting path interruption.

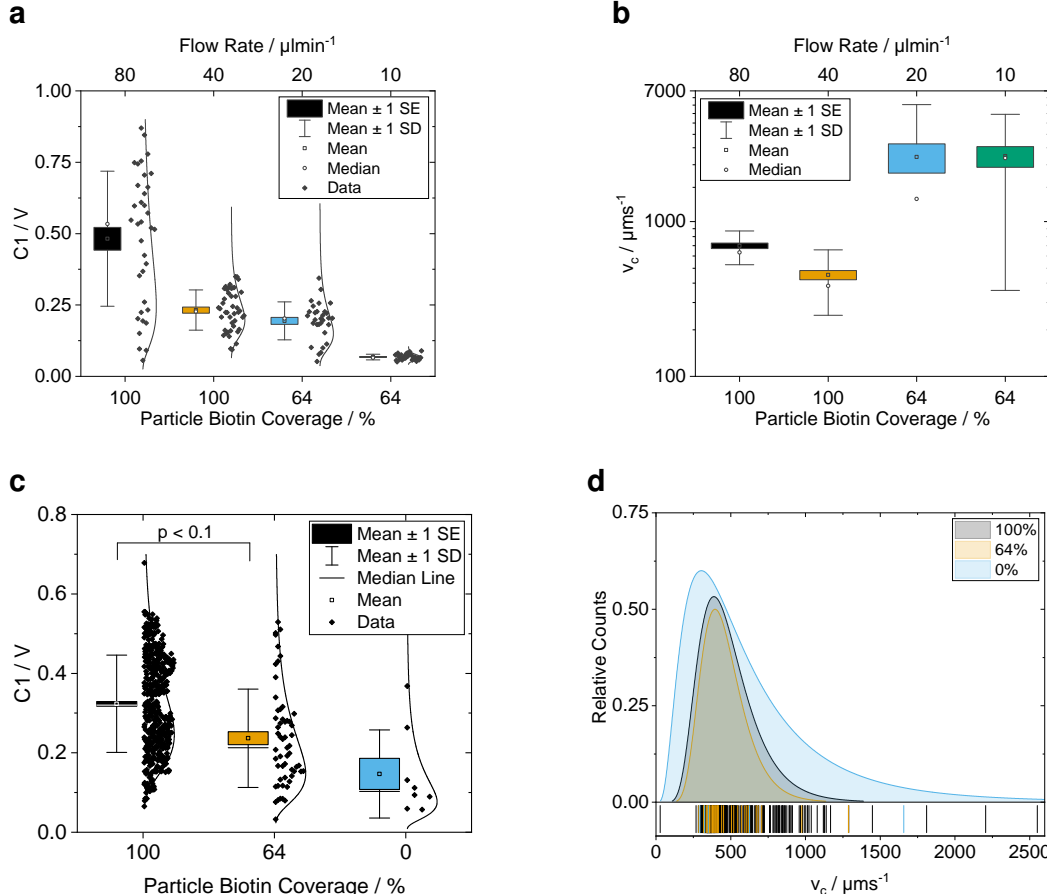


**Figure 26: Bead Coverage Assay with Magnetic Streptavidin Nanoparticles**

Magnetic flow cytometry data from 8  $\mu\text{m}$  polystyrene sphere which were biotinylated in different degrees and subsequently coated with BNF-Dextran-redF-streptavidin 100 nm MNPs (a,b) or SV0050 50 nm streptavidin MNPs (c,d). (a) Signal amplitude of the counts with various flow rates 1. 80  $\mu\text{L min}^{-1}$  2. 40  $\mu\text{L min}^{-1}$  3. 20  $\mu\text{L min}^{-1}$  4. 10  $\mu\text{L min}^{-1}$  (b) Reconstructed velocities of the respective populations. The 100 % biotinylation shows plausible velocities, whereas the 68 % sample can either be considered as noisy background or very weakly magnetized particles. (c) Signal amplitude with 80  $\mu\text{L min}^{-1}$ . A correlation between biotinylation degree and magnetic momentum can be assumed at a p-value  $p < 0.1$  (d) Velocity distributions of the samples. As postulated, the mean velocities do not differ, moreover, are enveloped by the blank sample.

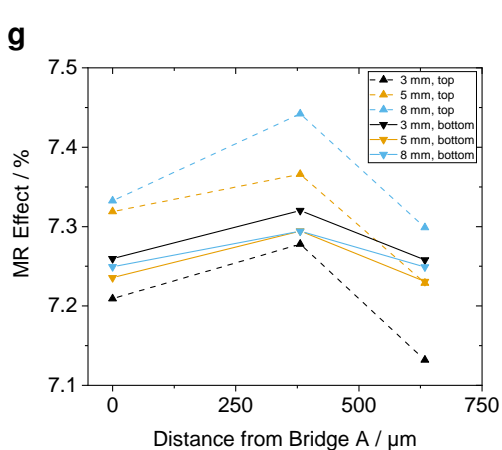
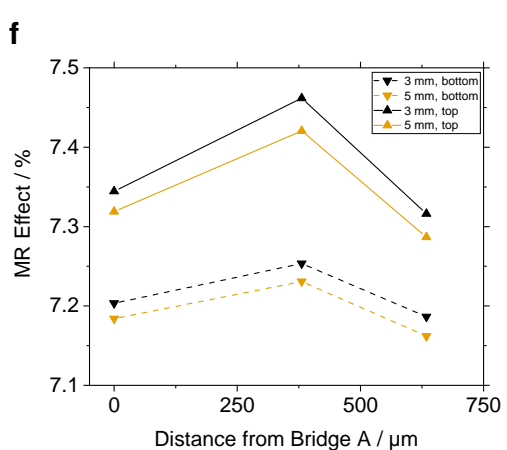
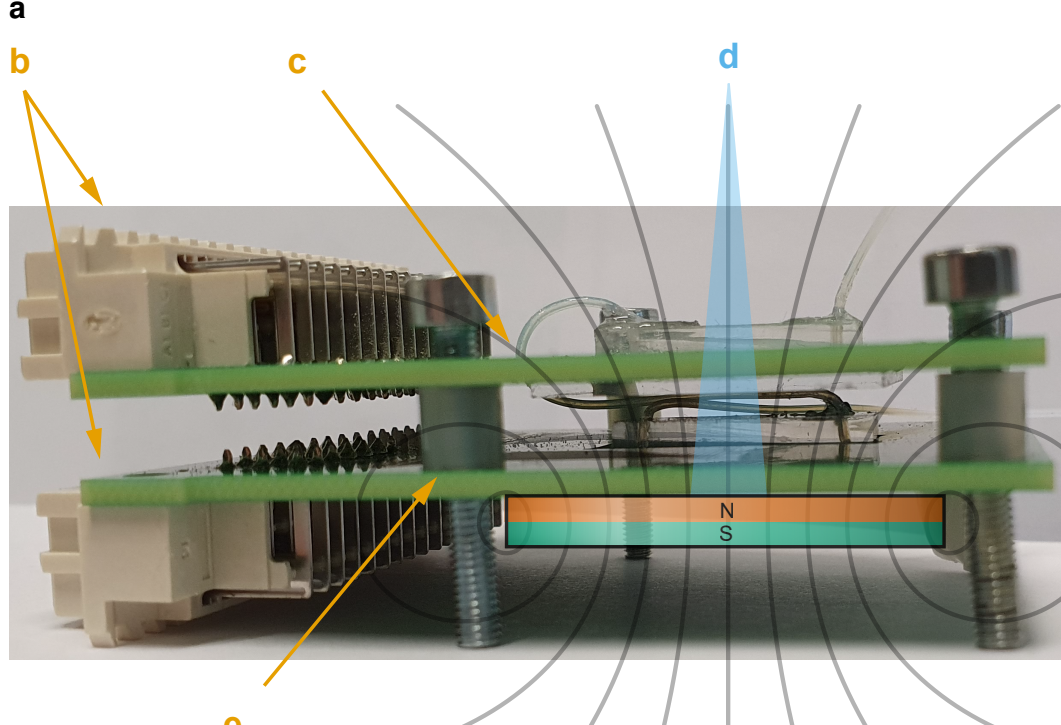


**Figure 27: Hysteresis Calibration for Stacked PCB Setup**

(a) Differential measurement setup: the system comprises of two separately assembled sensor PCBs (b) with nylon spacers (e) between the positional screws. (f) A hole with 3 mm diameter was drilled between the strip lines to connect the top chip outlet to the bottom chip inlet and minimize tubing length thereby. Schematically, a permanent magnet is placed below the bottom PCB. (d) The field line density respectively the area with negligibly differing field vectors is shown in the blue triangle. Because the adjustment is always carried out for a single bridge at once, this causes a systematic error.

The magneto-resistive effects of both sensors, calculated from their hystereses, are depicted for top and bottom sensors, respectively. Whereas the hysteresis was optimized for the centered sensor bridge (D or E) on the top sensor in (f), it was optimized for the bottom sensor in (g). Additionally, the height of the nylon spacers was varied from 3 mm to 8 mm but showed no statistical correlation.

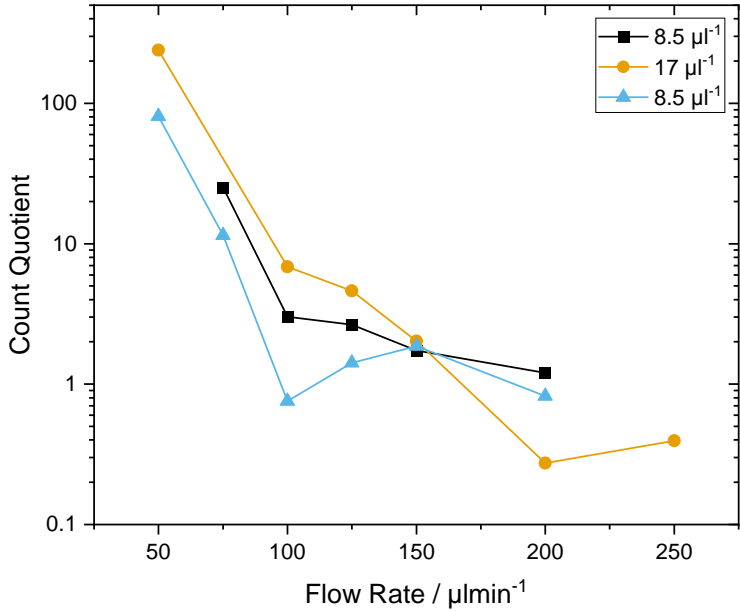
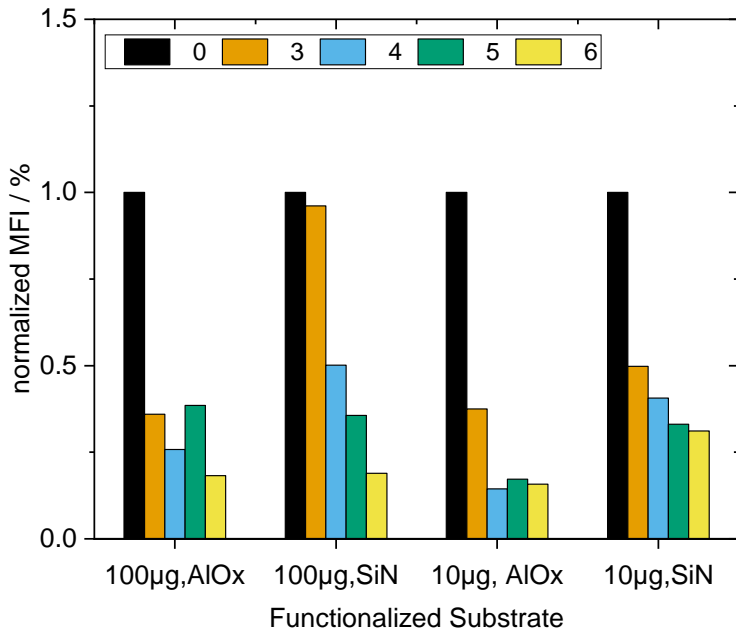


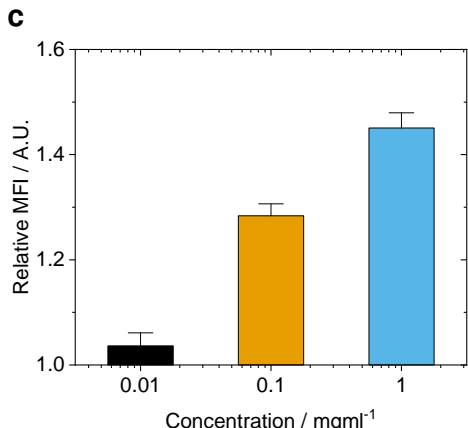
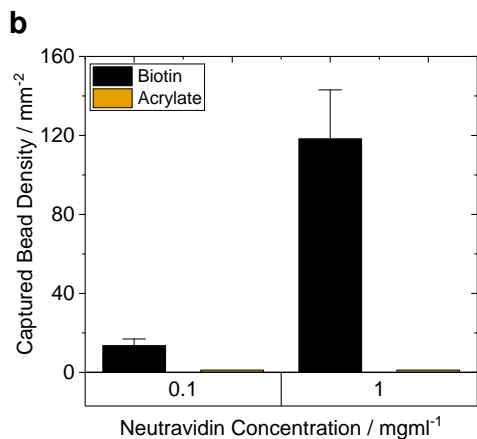
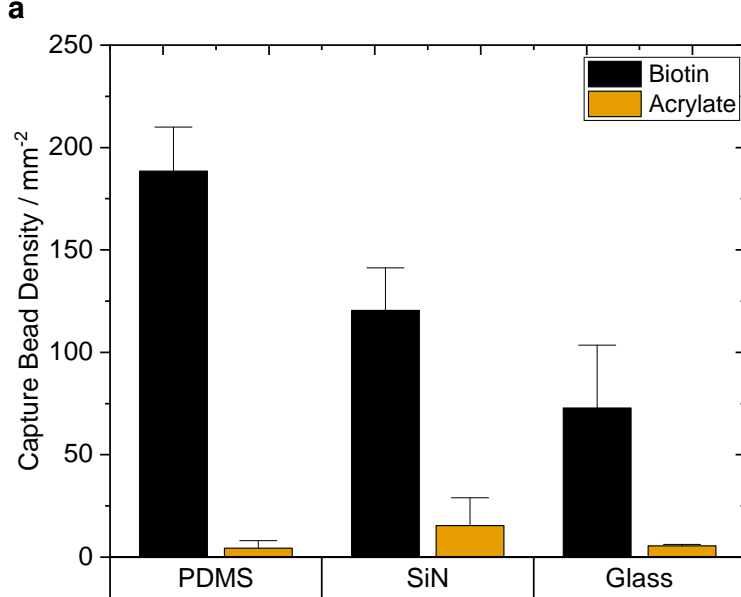
Figure 28: Optimal Differential Counting Flow Rate

Losses in different buffers and bead surfaces.



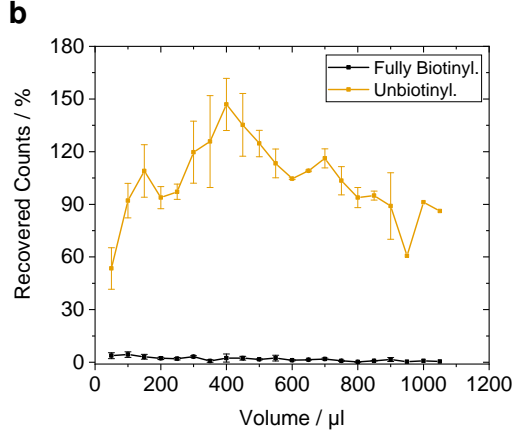
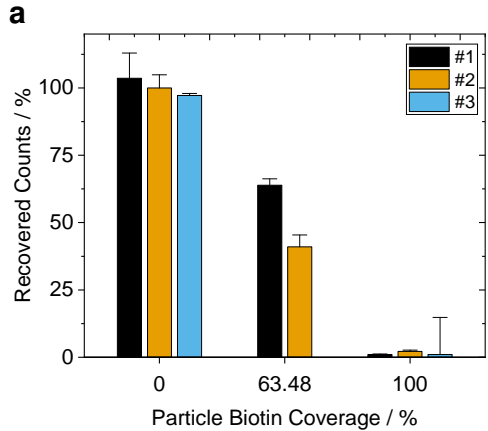
**Figure 29: Surface Adsorption Stability of Neutravidin on  $\text{Si}_3\text{N}_4$  and Aluminium oxide ( $\text{Al}_2\text{Ox}_3$ )**

Plate reader measurement with 3 mm x 3 mm  $\text{Si}_3\text{N}_4$  and  $\text{Al}_2\text{Ox}_3$  samples which were incubated with 100 µg and 10 µg streptavidin-atto488, respectively. The samples were subsequently washed with 200 µL PBS carefully. Fluorescence intensities were corrected with a blank substrate, the autofluorescence of PBS, and normalized eventually. Every surface reaches a mean fluorescence level of 28 % after few washing steps.



**Figure 30: Optical Bead Capture Assay and Titration Fluorescence Analysis**

(a) Density measurement of captured beads on the covalently functionalized surfaces of PDMS,  $\text{Si}_3\text{N}_4$  and glass. PDMS shows the most promising density. (b) Titration of neutravidin on covalently functionalized glass with a subsequent analysis by a bead capture assay. (c) Titration of streptavidin-atto488 on covalently functionalized glass with subsequent fluorescence microscope imaging. The scale indicated the fraction above the fluorescence signal of a blank microchannel.



**Figure 31: Reproducibility of Concentration Measurements with Saturated Neutravidin Surfaces**

Biological replicates of concentration measurements with the magnetic flow cytometer. The channel surface was modified with  $1 \text{ mg mL}^{-1}$  neutravidin over night. (a) Mean and SEM of  $C_{\text{const}}$  adjusted counts for various biotinylation degrees. (b) Time series of the mean from the three measurements on the left. Biotin-beads are captured completely, thus very few counts are detected. (—) The unbiotinylated sample shows the initial ascent due to the in ?? discussed error which is related to the filling of the magnetophoretic structures. (—)

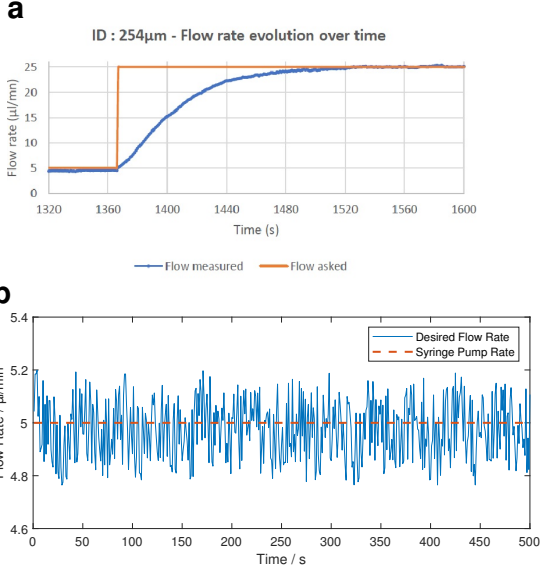


**Figure 32: Syringe Pump error sources**

Set flow rate: —, Real Flow Rate: —. The transient term of the NSE (??) was neglected in all simulations. However, a connected syringe pump retains a finite rise time (a) and a remaining “pulsation error” in steady state (b). In effect, an error adds to simulation and experiment. Therefore, any measurement can only be valid several ten seconds after the last flow rate change. (a) Exemplary, transient step answer of a syringe pump through a microtube with 254  $\mu\text{m}$  inner diameter. (b) Steady state flow rate error around the desired 5  $\mu\text{L min}^{-1}$  dispensing rate. A sinusoidal behavior caused by the microstepping can be observed. [104]

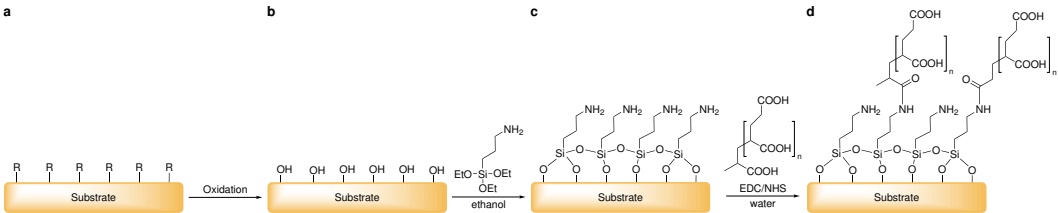


**Figure 33: General process chain of chemical surface modification**

Any substrate with various surface groups R (a) is oxidized to exhibit hydroxyl groups.(b). Then a silane SAM is attached (c) and subsequently modified by carbodiimide chemistry with PAA. (d)

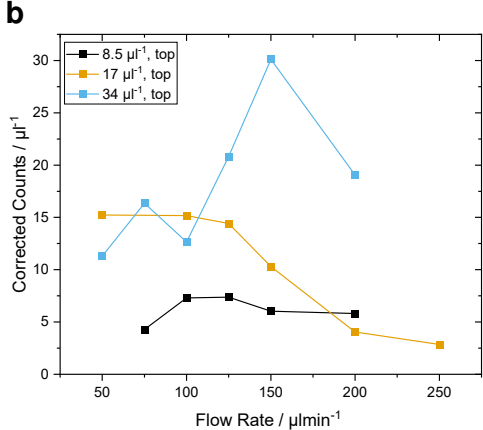
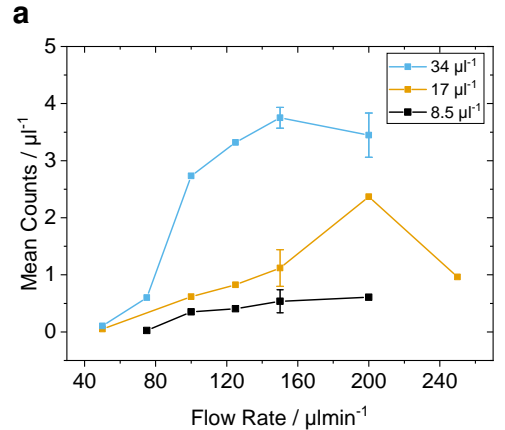


**Figure 34: Flow Rate Dependency of Differential Counting Setup**  
(a) Optimized for top sensor (b) Optimized for bottom sensor

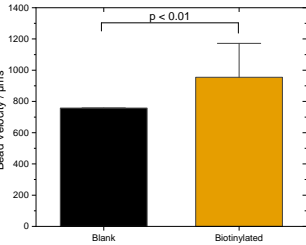


**Figure 35: Measured Bead Velocity**

Not sure what to say about velocity itself. Maybe remove completely,  $p < 0.01$

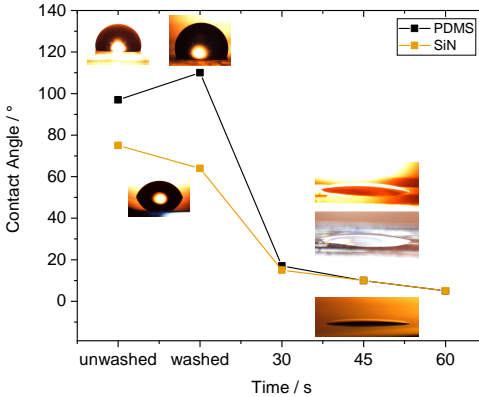


**Figure 36: Hydrophobicity Analysis of PDMS under Plasma Exposure**

For an optimal plasma bond to glass,  $\text{Si}_3\text{N}_4$  and PDMS, the contact angle was measured after treatment. The initial decrease until 45 s declares the optimum around this time. Longer times should be avoided consequently to prohibit further surface damages by reactive ions.